ORIGINAL PAPER

Effect of Mn²⁺ Substitution into the Host Lattice of ZnO via sol–gel Route for Boosting the Dye-Sensitized Solar Cells Performance

Deepak Kumbhar[1,2,7] · Sagar Delekar[2] · Sarita Kumbhar[3] · Ananta Dhodamani[4] · Namdev Harale[5,6] · Rekha Nalawade[7] · Avinash Nalawade[7]

Abstract
In this study, Mn²⁺ ion is doped in ZnO lattice framework at 1, 3 and 5 wt % by a simple and low-cost sol–gel route to attain improved optoelectronic response. The structural investigation by XRD and Raman analysis explores the formation of hexagonal wurtzite framework with variations in lattice parameters comprising peak intensities favors the Mn doping. The extent of doping was supported by EDS analysis, while XPS confirms doping in + 2 chemical state. The optical investigation by UV–visible and PL provides prominent peaks that also specify peak shifting in order of doping level, while the significant hexagon-shaped nanoparticle (NP) formation was deduced in SEM and TEM micrographs. These proficient ZnO NPs have been deposited on fluorine-doped tin oxide (FTO) conducting glass plate by doctor-blade technique to get photoanodes. The electrical performance of these photoanodes especially photocurrent generation was investigated under standard AM 1.5 one sun illuminations. The highest photoconversion efficiency was attained for 3% Mn-doped ZnO photoanode after xanthene-based organic dye sensitization with output efficiency (η%) of 0.25% higher than 0.03% of bare ZnO. The comparable ionic radii with exactly half-filled 3d orbital simply overlap with the ZnO valence bond responsible for enhanced overall structural and optical properties that beneficial for DSSCs performance.

✉ Deepak Kumbhar
deepak.que@gmail.com

✉ Sagar Delekar

✉ Avinash Nalawade
avinashnalawaderes@gmail.com

1 Department of Chemistry, Raje Ramrao Mahavidyalaya, Jath, Sangli, Affiliated To Shivaji University, Kolhapur, M.S., India

2 Department of Chemistry, Shivaji University, Kolhapur, M.S., India

3 Department of Physics, Rajarshi Chhatrapati Shahu College, Kolhapur, Affiliated To Shivaji University, Kolhapur, M.S., India

4 Department of Chemistry, Rajarshi Chhatrapati Shahu College, Kolhapur, Affiliated To Shivaji University, Kolhapur, M.S., India

5 Chemical Engineering and Process Development Division, National Chemical Laboratory, Pune, M.S., India

6 Sadguru Gadage Maharaj College Karad, Satara, Affiliated To Shivaji University, Kolhapur, M.S., India

7 Department of Chemistry, Lal Bahadur Shastri College, Satara, Affiliated to Shivaji University, Kolhapur, M.S., India

Introduction

In the last few decades, elevation in international energy requirement and issue of global warming encouraged human to move from non-renewable to renewable energy sources. So, energy securities with taking care of global warming are the driving factors. The reports disclosed global energy usage oil (37%), coal (27%) and natural gas (20%). So these resources are not much an adequate for extensive period that can be probable only up to 40 years as calculated from daily consumption formula (Aarrestad 1990; van Zalk and Behrens 2018). Electrical energy is the merely chief energy source that can satisfy all needs of human that can be produced via solar energy as a clean source (Al-Alwani et al. 2016; Grandell et al. 2016). So, the photovoltaic (PV) module having solar cells that transform solar energy into electricity is keen interest. Until now researchers developed various materials and modules upgraded generation after generation (Fakharuddin et al. 2014). The first-generation PV module relies on single-function Si wafers, whereas second generation made by polycrystalline-Si or amorphous-Si

(a-Si), CdTe/CdS(CdTe) materials. Third-generation modules are cheap and flexible with advance technologies that include specifically dye-sensitized solar cell (DSSCs), perovskite and organic solar cells (Badawy 2015; Green 2002; Sharma et al. 2017). Amongst them, DSSCs fascinated a lot due to low cost, simple construction and good output. Such a well-constructed module was first put forth by O'Regan and Grätzel in 1991 (1991). This typical DSSCS made from mesoporous TiO_2 photoanode, metal-based dye (Ru) that adsorbed on TiO_2 surface to capture maximum light and iodide/triiodide ion electrolyte with Pt or carbon as a counter electrode. The maximum light-to-electricity output conversion efficiency (η) is acquired to be 12.3% but struck in several curbs (Li et al. 2009; Son et al. 2018; Ye et al. 2015). So other wide band gap semiconductor metal oxides like ZnO, Nb_2O_5, $SrTiO_3$ and SnO_2 are also best alternative material for TiO_2 but still under the progressive stage to capture optimal output efficiencies (Bhardwaj et al. 2018; Jayachandraiah and Krishnaiah 2017; Putri et al. 2018; Sharma et al. 2012; Shrama et al. 2014). From these materials, ZnO seems to be the finest one retaining wide band gap ~ 3.37 eV with ~ 60 meV exciton binding energy, and variety of other favorable qualities (Sushma and Girish Kumar 2017). ZnO is advantageous than TiO_2 exhibiting higher electron mobility, huge chemical stability, low toxicity, biodegradability and greater electrochemical coupling ecoefficiency. The DSSCs performance of particular semiconductor relies on numerous aspects comprising of structural, morphological, optical and electrical attributes. In ZnO, these features having potential tuneable and consequently highest conversion efficiency (η) were recorded to be 7.5%. But its efficiency is nearly half than TiO_2, and it is still under the progressive stage.

So, strategies engaged to boost its efficiency include hierarchical structure fabrication, innovative thought of assembling, anticipation of Zn^{2+}/dye aggregation, utilization of nanocomposites, reduction in recombination reactions and exploitation of diverse dyes (Shrama et al. 2014; Vittal and Ho 2017). To achieve this, ZnO already fabricated in numerous forms that deal with variations in shape, surface area, porosity and pore size. The diverse methods already engaged to form nanowires, nanorods, nanobridge, nanorings, nanocages, nanocombs, nanobelts, 3D nanomaterials and many more to acquire ideal outcomes (Bhakat and Singh 2012; Sharma et al. 2017; Ansari et al. 2018). However, another hopeful way is effective in doping in ZnO lattice with suitable cations to tune its features (Sengupta et al. 2016). It modifies the electron flow by implanting new energy level in between conduction band and Fermi level (Khan et al. 2017). It is already revealed that cations B, Mg, Ga, Sn, Ag, Li, Eu, Al doping give efficiencies (η) 7.2%, 4.11%, 4.02%, 3.79%, 2.02%, 1.23%, 0.50%, 0.298%, respectively (Mahmood et al. 2014; Kim et al. 2012; Lanjewar and Gohel 2017; Ye et al. 2010; Raj et al. 2013; Aksoy et al. 2018; Felipe et al. 2018,

Tao et al. 2012). Also aluminum–boron-co-doped ZnO has the highest efficiency reported to be 1.84% (Kumar et al. 2013). Similarly, incorporation of transition metals also works operative due to electron enrichment in d-orbital and having alike ionic radii favors the doping probability efficiencies (Nithya et al. 2015; Shah et al. 2017). The results reported by dopants Co, Cu, Fe and Mn give output efficiencies of 0.557%, 0.647%, 0.465%, 0.251%, respectively, under operative conditions (Fabbiyola and Kennedy 2019), as in former studies we worked with Cu and Co dopant that urges to study with Mn. (Deepak et al. 2019; Kumbhar et al. 2020).

In contrast to other, Mn is probably preferred due to half-filled d^5 electrons at t_2g level, which can effortlessly overlap with ZnO valence band. This half-filled orbital has the highest possible magnetic moment that makes it stable polarized state. Besides, theoretical interpretation concluded that Mn-doped ZnO appears to be ferromagnetic with higher Curie temperature than room temperature (Singh et al. 2014; Yang and Zhang 2013). In this doping approach, the concentration of dopant also plays a critical role that decides working competence for a specific module. Specifically, alteration in band gap ruled by doping level and study revealed that shrinkage in band gap perceived at low concentration, while higher concentration enhances band gap (Aimouch et al. 2018; Mondal et al. 2013). Therefore, our study emphasized on optimal doping of Mn to achieve enhanced outcomes than native ZnO. As many researchers worked with this dopant and applied it in several modules, Hao et al. synthesized series of Mn-doped ZnO nanoparticles by hydrothermal route. Its optical absorption is given blue shifting, while PL spectra point out doping results in band-edge UV emission (Hao et al. 2012). Also the effect of Mn doping on structural and sensing properties of ZnO was studied by Mao et al. Here the gas sensing characteristic was greatly impacted by Mn-doped ZnO (Mao et al. 2014). Ton-That et al. studied crystallographic as well as optical characteristics of Mn-doped ZnO nanoparticles synthesized by a sol–gel method (Ton-That et al. 2012). Rekha et al. gave various aspects of Mn-doped zinc oxide including structural, optical, photochemical and antibacterial characteristics (Rekha et al. 2010). Jayakumar et al. reported the synthesis of 2 and 5 at% Mn-doped ZnO nanoparticles by a co-precipitation method to give wurtzite crystal structure with the change in unit cell volume with a concentration of Mn doping (Jayakumar et al. 2006). Emission of Mn-doped ZnO NPs was developed by mechanochemical processing studied by Sabri and co-workers. The experimental results reveal its various structural features (Sabri et al. 2012). So Mn doping enhances the overall properties of ZnO, which can possibly boost the photoelectric performance of DSSCs. As E. Akman studied its performance under N-719 dye that gives output efficiency up to 4.20% (Akman 2020), these frequently used N719, N3 dyes were based on Ru metal engaged to catch superior

efficiencies, though they were badly affected by deprived stability, lethal nature and overpriced to apply it extensively. Otherwise highly conjugated metal-free organic dyes have great ability in the UV–visible region. Therein xanthene dyes eminently attracted the attention of researchers due to cost-effectiveness, lower acidity, less aggregation, abundant anchoring groups and avoided Zn2þ/dye aggregation (Guillén et al. 2011). That perhaps alters the performance on cutting-edge superior mode. So in this study simply operative *sol–gel* approach was performed to get Mn-doped ZnO at various low doping levels and evaluated by structural, morphological and optical platforms, as in higher doping excess of charge carriers shifts the Fermi level inside the conduction band. The photoanodes were prepared to catch electrical outcomes by formerly known doctor blade technique. Afterward, economic and eco-friendly xanthene dyes employed for current–voltage measurements were done at standard AM 1.5 one sun illuminations (100 mW/cm^2) to execute maximum quantum efficiency.

Experimental

Materials

In the experimental work, we used zinc acetate dihydrate ($C_4H_{10}O_6Zn$, Sigma-Aldrich, German 99.99%), manganese acetate tetrahydrate ($C_4H_{14}MnO_8$, Sigma-Aldrich, German, 99.99%), SDS, i.e., sodium dodecyl sulfate ($NaC_{12}H_{25}SO_4$, SD Fine, India > 98%), ammonium solution 25% (NH_4OH, SD Fine, India > 98%), ethyl cellulose ($C_{20}H_{38}O_{11}$, Sigma-Aldrich, German), α-terpineol (Sigma-Aldrich, German 90%) and alcohol (C_2H_5OH, S. D. fine, India 99.9%) were used of analytical reagent grade without further treatment.

Synthesis of ZnO and Mn-doped ZnO NPs by sol–gel method

To synthesize ZnO NPs by sol–gel route 0.2 M zinc acetate dihydrate solution was prepared in double-distilled water (DDW). In this, 0.02 M of sodium dodecyl sulfate (SDS) was added with constant stirring for 15 min. In this homogenous solution, ammonium hydroxide was mixed dropwise until pH reaches to the basic condition, i.e., 8.0 ± 0.1. The formation of zinc hydroxide sol takes place that placed at 80 °C for 9 h for gelation. This obtained gel was dried to get the powder and further calcinated at 400 °C for 3 h in a muffle furnace outcome in ZnO NPs. Similarly, Mn-doped ZnO (Mn-ZnO) NPs were prepared by taking manganese acetate tetrahydrate in similar zinc acetate dihydrate solution as per calculated doping amounts of 1%, 3% and 5% wt% composition.

Preparation of Thin Films

After the formation of NPs for measurement of electrical response fabrication of photoanodes is necessary. So, a simple doctor blade technique was employed to construct photoanodes (Kim et al. 2017). In this, ZnO NPs were dispersed in ethyl cellulose and alcohol. Then, formed suspension was sonicated for 30 min and a suitable quantity of α-terpineol was added into it. This suspension was now stirred for 2 h, and finally, the upper organic layer was decanted. The remained viscous paste was deposited on the cleaned surface of the FTO glass substrate. After deposition films were dried and annealed at 350 °C for 2 h in a muffle furnace and used as the further study.

Characterizations

X-ray diffraction (XRD) was characterized by X-ray diffractometer of Bruker AXS Analytical Instruments Pvt. Ltd., Germany, D2 phaser Model (CuKα radiation, $\lambda = 1.5418$ Å). Here, the samples were placed on zero diffraction plate sample holder, and XRD patterns were recorded at RT. Raman spectra also were used for further verification in the recording range of 200 to 600 cm^{-1} by Raman spectrophotometer of Bruker Multi-RAM, Germany, fitted with an Nd:YAG laser source having excitation wavelength of 1064 nm with resolution 4 cm^{-1}. The morphological investigation was done using scanning electron microscopy (SEM) of JEOL-JSM-6360, Japan, working at 20 kV after powder sample placed stage. For the transmission electron microscopy (TEM) by TECNAI F20 Philips, the powder sample put on copper grid. Compositional analysis doped sample verified by X-ray photoelectron spectroscopy (XPS of VG Microtech ESCA 3000) by exciting the sample surface using monoenergetic Al kα X-rays. Diffuse reflectance spectroscopy studies (DRS UV–Visible) absorption spectra were recorded using Lab India UV-3092 spectrophotometer by placing the sample in sample holder, while normal UV–visible spectra were recorded by LAMBDA 950 spectrophotometer in the range of 300–800 nm. Also, photoluminescence (PL) spectra were obtained by spectrofluorometer FP8200, Jasco, consisting of He-Cd laser excitation source with excitation wavelength 300 nm at RT. Fourier transform infrared spectroscopy (FTIR) data were recorded from FTIR Spectrometer 4600, Jasco. For FTIR, the prepared materials were dispersed in KBr solution water and spectra were recorded in the range 4000–500 cm^{-1}. Electrochemical impedance spectroscopy (EIS) and current–voltage (I-V) measurements were taken using a Keithley source meter (model 2460) in photoelectrochemical cell prepared in iodide redox electrolyte with active photoanode and Pt-deposited FTO plate acts as counter electrode.

Results and Discussion

XRD Rietveld Analysis

The X-ray diffraction patterns of ZnO and 1, 3 and 5% Mn-ZnO NPs were obtained by CuKα (1.54056 Å) radiation shown in Fig. 1. The distinct peak patterns of samples demonstrate the formation of hexagonal wurtzite-type crystal structure. Although these peaks are in well concert with powder diffraction standard (JCPDS), data belonging to structural Card No. 36–1451 with relevant planes point out a wurtzite-type hexagonal structure with preferable orientation along (100), (002), (101), (102), (110), (103), (112) crystalline planes (Liu et al. 2014; Mittal et al. 2016). The prominent intensity peaks also suggest the high crystallite nature of the samples without any other diffraction peaks. It exposes the absence of impurities and no any secondary phase formation. So, it shows the substitution of Mn^{2+} ions in place of Zn^{2+} sites, which is fruitful without modifying the core crystal structure of ZnO lattice by sol–gel route. However, minor decline in peaks additionally supports this substitution in ZnO host lattice site.

For comprehensive investigation, XRD data further inspected under Rietveld refinement particularly specified in Fig. 2 were performed through FullProf program. The obtained output data comprise structural parameters, R factors, bond lengths, bond angles, which are summarized in Table 1. The χ^2 value implies virtuous fitting suitable for assessment of all parameters. It also guides that Mn is well incorporated into ZnO structure with certain makeover in a-axis and c-axis parameters associated with standard a = 3.25 (Å), c = 5.206 (Å) values by virtue of doping. It is further meant for exact measurements of bond length and
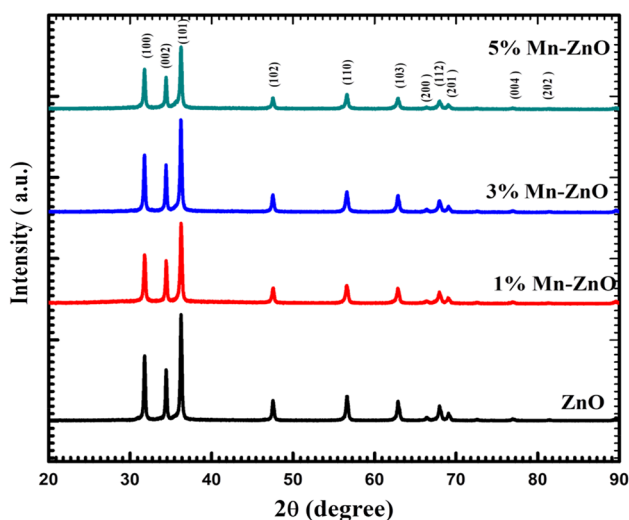
bond angles the structure visualized in three-dimensional mode in VESTA software. It also offers Wyckoff position 2b for Zn^{2+} and O^2 atoms with 0.333, 0.666 values for x, y atomic coordinates. The average crystallite size 'D' of the samples was calculated using the Debye–Scherrer formula, i.e., $D = 0.9\lambda/\beta \cos \theta$, where 'λ' is the wavelength of X-ray (1.5406 Å), 'β' the full width at half-maximum in radian and 'θ' the angle of diffraction (Undre et al. 2018). It clearly elucidates some reduction in crystallite size with regard to Mn doping owing to lesser radius of the Mn^{2+} ion (70 pm) with respect to the Zn^{2+} ion (74 pm) (Parthibavarman et al. 2016; Shatnawi et al. 2016; Singh et al. 2017). Such reform in parameters and crystallite size only perceived at lower doping level, while contrasting results were observed at higher doping level (Bonifácio et al. 2017; Jayanthi and Chawla 2010).

Raman Analysis

Structural investigation by XRD was supported by Raman spectra as given in Fig. 3. It provides peaks at 326, 400, 433, 572, 589 compiling to A_1 (TO), E_1 (TO), E_2 (high), E_1 (low) and A_1 (low), respectively. The E_2 (low) mode involves Zn sub-lattice motion besides high intensity of the E_2 (high) mode defines that samples have a good hexagonal wurtzite structure. The E_2 (high) peaks in Mn-ZnO expose that doping never distorts the basic ZnO crystal lattice (Bhardwaj et al. 2018; Putri et al. 2018). However, fluctuating its peak intensities attributed to doping conceive oxygen vacancies (VO) and zinc interstitials (Zn) defects at A_1 (LO) and E_1(LO) modes of ZnO. Also, the A_1 (TO) with E_1 (TO) mode was recognized at 326 and 400 cm^{-1} revealing variation in strength of lattice bond. Overall, Mn doping induces several broadening with alteration in intensities as a result of minor change in mass as well as included strain devoid of ZnO framework (Jayachandraiah and Krishnaiah 2017; Paul et al. 2016; Shrama et al. 2014). Here suppressed peak patterns and some instrumental noise were restricted to separate sharp peak intensities.

SEM and EDS Analysis

After structural investigation, morphological characteristics of prepared samples were studied through SEM micrographs under 30,000 magnifications as given in Fig. 4a. It appears to be formation of identical particles having smooth surfaces with perfect boundaries comprising certain agglomerations. The particle size distributions in samples were approximately computed in between 50 to 65 nm and varied with Mn doping levels because of Mn having less ionic radii than Zn. So it also suggests the successful doping of Mn in ZnO lattice with specific size change (Mahroug et al. 2018; Shatnawi et al. 2016).

Fig. 1 XRD patterns of pure ZnO and 1%, 3%, 5% Mn-ZnO NPs
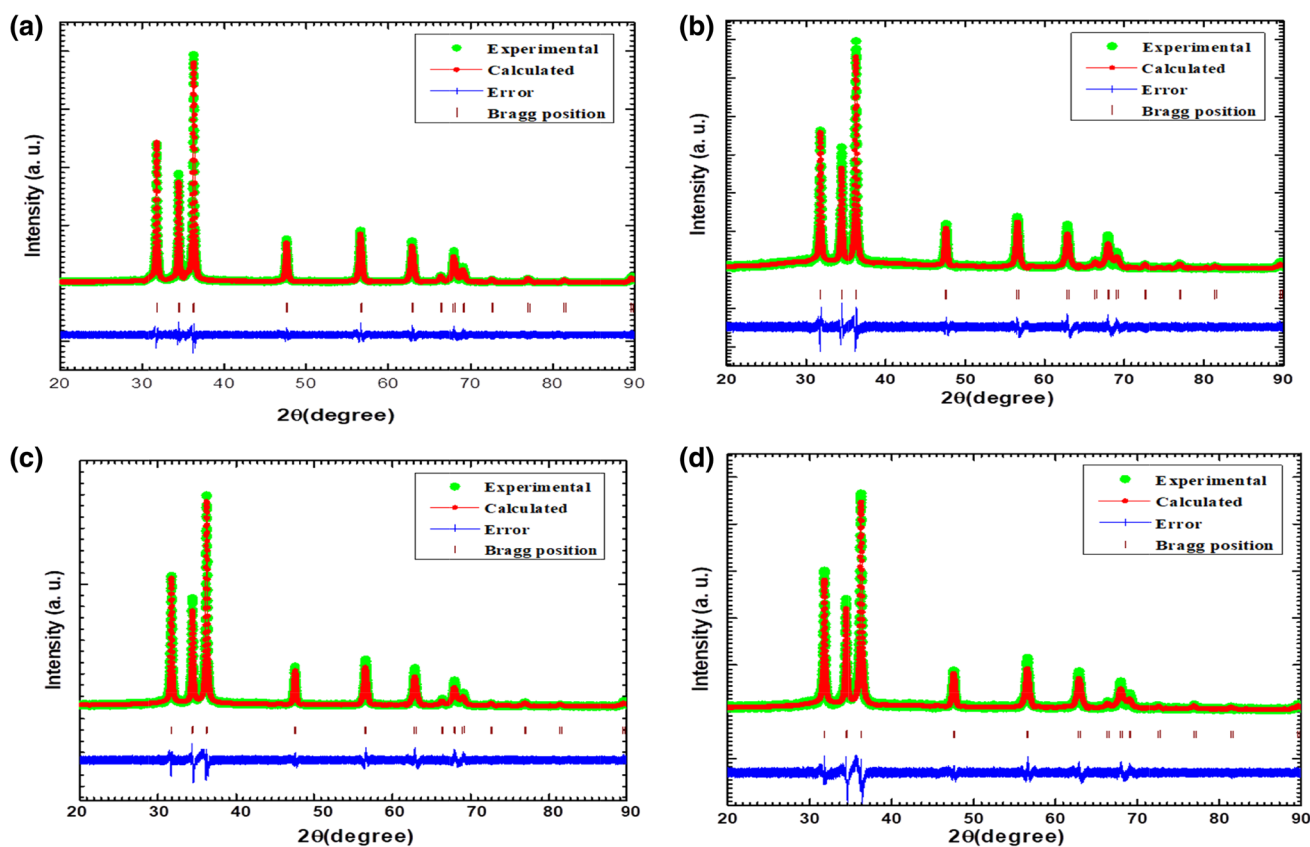
Fig. 2 Rietveld refinement patterns of (**a**) ZnO and (**b–d**) for 1, 3, 5% Mn-ZnO samples

Table 1 Cell parameters, Rietveld refinement factors, bond lengths, bond angles and crystallite size of ZnO and 1, 3, 5% Mn-ZnO

Sample	Cell parameters		R factors							Zn–O (Å)	Zn–O-Zn (degree)	Strain $\varepsilon \times 10^{-4}$	D (nm)
	a (Å)	c (Å)	v (Å)^3	Rp	Rwp	Rexp	χ^2	Rb	Rf				
ZnO	3.250	5.207	47.657	13.7	17.1	13.65	1.58	0.356	0.328	1.95	109.11	0.026	43
1% Mn-ZnO	3.251	5.2	47.664	22	23.9	15.26	2.45	0.838	0.519	1.952	109.121	0.025	42
3% Mn-ZnO	3.253	5.207	47.75	19.7	22	13.76	2.55	1.27	0.822	1.952	109.114	0.022	38
5% Mn-ZnO	3.253	5.207	47.721	28	28.3	17.83	2.51	1.91	1.086	1.987	109.114	0.019	36

Further detail elemental compositions inspected through EDS (Fig. 4b) elucidate the existence of appropriate elements below 10 keV, i.e., presence of Zn, O and Mn atoms in corresponding ZnO- and Mn-doped samples. So, EDS data validate Wt% proportion of Mn in ZnO as summarized in Table 2 and also proved the absence of any other impurities.

TEM Analysis

As SEM micrographs provide limited information of particle nature, then characteristic 3% ZnO sample is investigated under transmission electron microscopy as results given in Fig. 5a,b. It displays particles are in proper hexagonal-shaped discs and having good transparency under electron gun. These hexagonal disks or plates have average particle size of 55 to 60 nm. Here long chains of SDS surfactant control the growth of crystals to acquire nanohexagonal morphology. It can be exposed as sulfonic group in anionic form of SDS preventing the progression in c-axis direction (0001) and pushing the growth toward (1010) to form hexagonal disk shapes. Such particle nature is also attained by different research groups using alternative synthetic method (López et al. 2017; Tuyen et al. 2009). SAED patterns as shown in
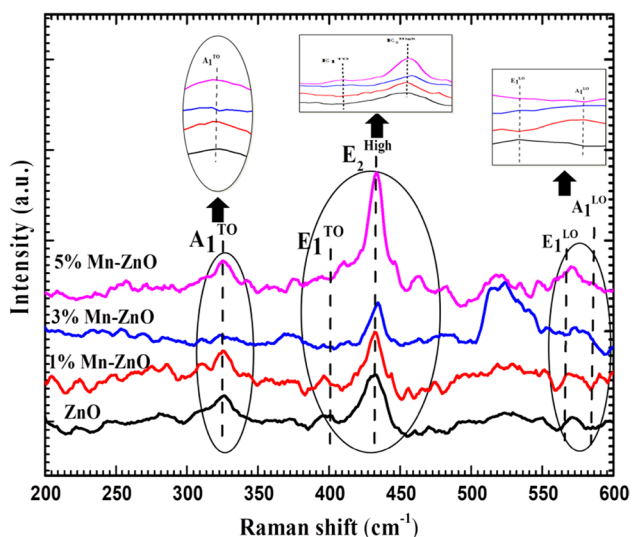
Fig. 3 Raman spectra of ZnO and Mn-ZnO NPs

Fig. 5c also support hexagonal wurtzite structure of ZnO similar in XRD, Raman analysis. The patters indicate sharp and bright nature of diffraction planes (100), (002), (101), (102) to validate space group of P63mc and JCPDS card No. 36–1451.

XPS Analysis

The XRD and EDAX results already revealed that there are no other peaks observed and Mn is doped in ZnO lattice; however, XPS technique offers how Mn incorporated into Zn matrix. It offers composition of manganese atom in

Mn-doped ZnO NPs. Representative 3% Mn-doped sample was used that illustrates the existence of Zn, Mn, and O atoms with chemical purity. In Fig. 6a, the full XPS survey represents the characteristic peaks of Zn, Mn, O with adventitious 'C' elements confirming the Mn incorporated in ZnO host lattice. The detail oxidation states were inspected by fine scan around every element. The obtained results are given in Fig. 6b–d with regard to Zn 2p, Mn 2p, and O 1 s, respectively.

In core-level Zn 2p spectra, strong peaks located at 1023 eV and 1045 eV correspond to Zn 2p 3/2 and Zn 2p1/2 states, respectively. It specifies that Zn conserves its + 2 oxidation state and no any Mn-Zn–O clusters were formed (Shatnawi et al. 2016). The XPS peaks of O1s revealed that there is existence of multicomponent oxygen on the surface. The fitting curve explains the presence of three components centered at 531.3 eV, 532.8 eV and 534.2 eV. The lower energy peak of 531.3 eV is due to lattice oxygen and peak around 532.8 eV is of oxygen deficiency in Mn-doped sample matrix. The last peak 534.2 eV is attributed to chemisorbed oxygen of superficial hydroxyl, H_2O or O_2 and – CO_3 (Liu et al. 2013). The distribution of Mn in the sample was

Table 2 Composition of ZnO and Mn-ZnO NPs

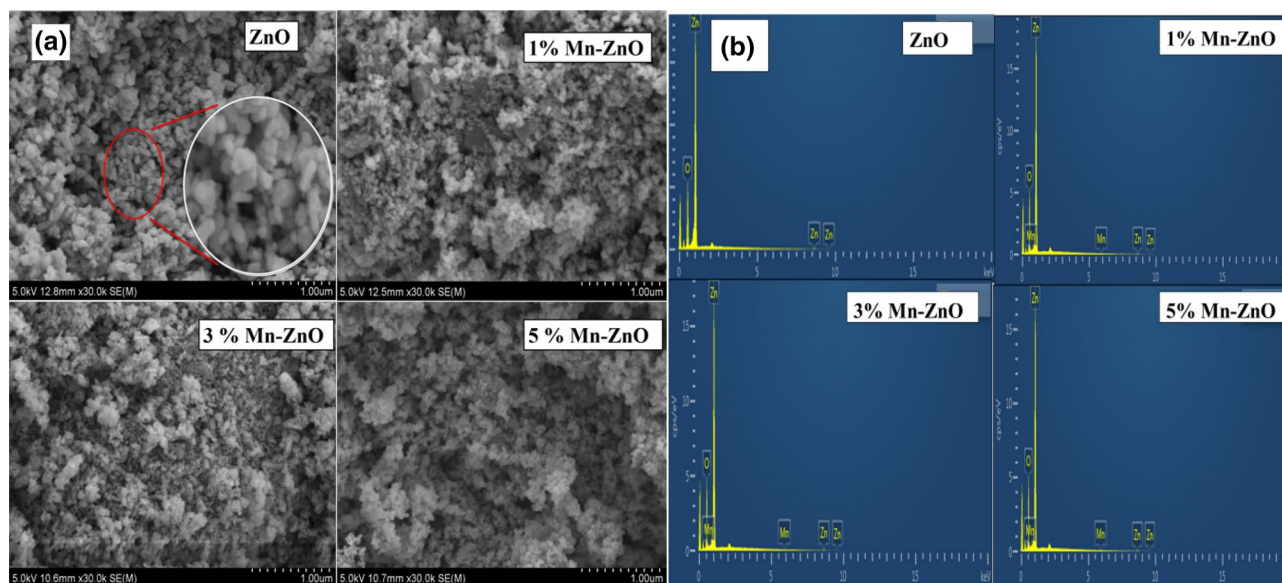| Sample	O (Wt%)	Zn (Wt%)	Mn (Wt%)
ZnO	16.84	83.16	–
1% Mn-ZnO	16.23	82.43	1.34
3% Mn-ZnO	16.60	80.12	3.28
5% Mn-ZnO	17.20	78.54	4.26

Fig. 4 SEM and EDS of Mn-ZnO NPs (**a**) SEM of ZnO and 1, 3, 5% Mn-ZnO NPs (**b**) EDS patterns of ZnO and 1, 3,5% Mn-ZnO NPs
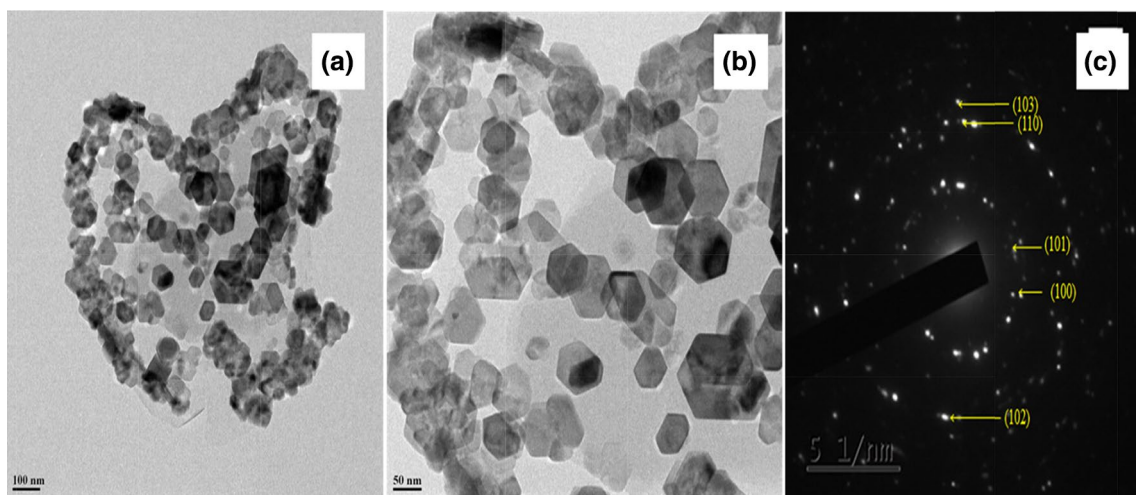
Fig. 5 (**a**, **b**) TEM images of typical ZnO sample (**c**) SAED pattern
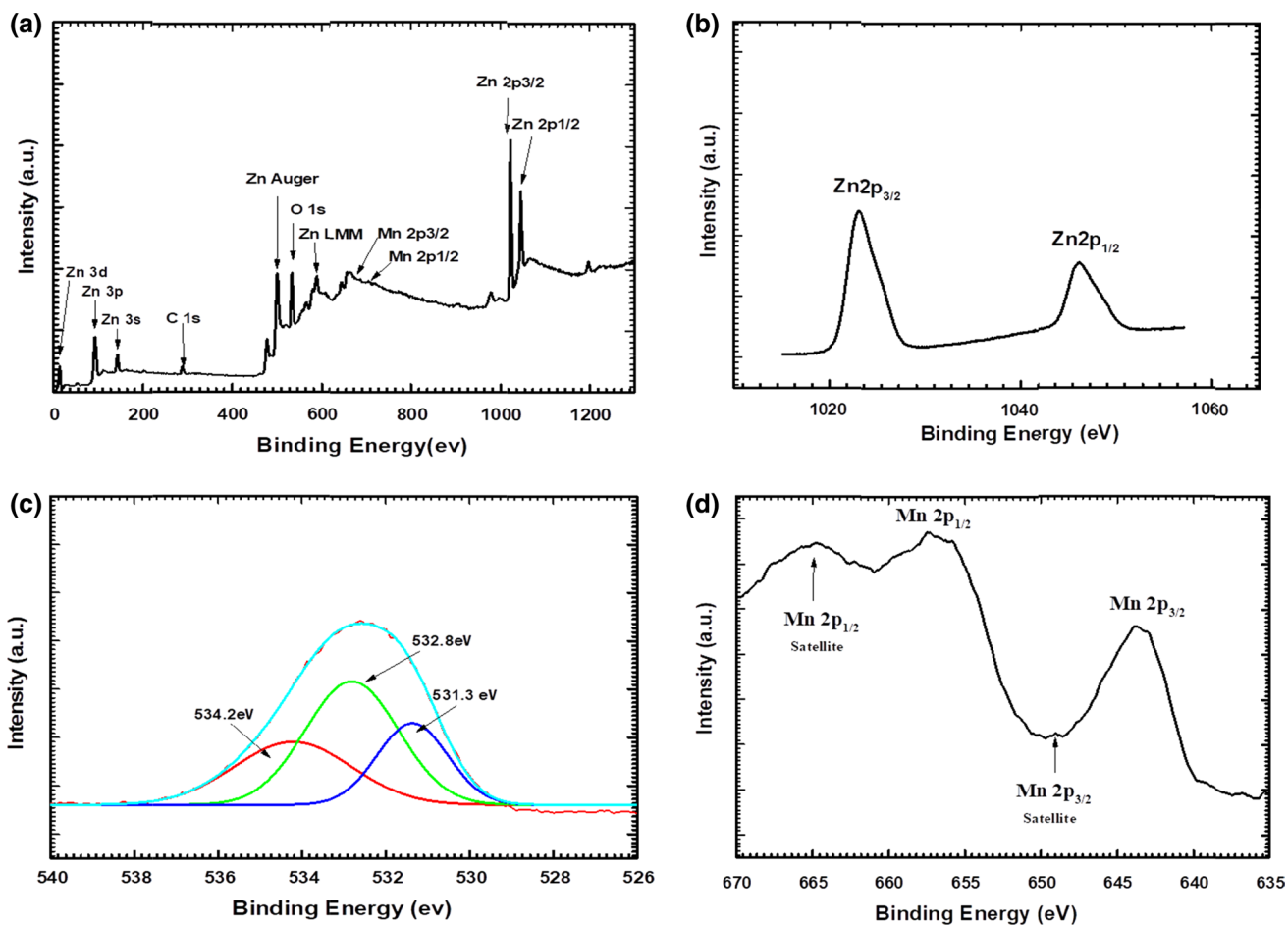

Fig. 6 XPS spectra of 3%Mn-ZnONPs. (**a**) Survey spectrum (**b**) core-level spectra of Zn 2p (**c**) core-level spectra of O 1 s and (**d**) core-level spectra of Mn 2p, respectively

studied by core spectrum of Mn 2p. The spectrum confirms the presence of Mn 2p3/2, 2p1/2 at 643.7 eV and 655.8 eV, respectively. It concludes that Mn atoms are bounded and exist in Mn^{2+} valence state (Ganesh et al. 2017).

FTIR Analysis

The FTIR bands of stretching and bending modes of Cu–ZnO resemble with ZnO as given in Fig. 7. The measured range of 500 to 4000 cm^{-1} consists of the absorption bands near to 3500 cm^{-1} ascribed to O–H stretching mode. While the absorption peaks in the range of 1580–1691 cm^{-1} are attributed to Zn–O stretching mode. Also absorption peak ~ 1100 cm^{-1} associated with the OH bending mode and the peaks in the range from 429 to 881 cm^{-1} are attributed to the metal-oxide (Zn–O or Mn–O) stretching and vibrational modes, which reveal the incorporation of Mn ions into ZnO hexagonal lattice. The minor shifting of peaks toward greater wavenumber, i.e., blue shifting with deviation in intensities also elucidates Mn doping into ZnO lattice site (Sharma et al. 2017; Viswanatha et al. 2004; Hao et al. 2012; Jayanthi et al. 2010; Shohany et al. 2018).

PL Analysis

The quality of crystal and the existence of defects due to doping are examined by photoluminescence emission spectroscopy (Ponnusamy et al. 2016). PL spectra recorded at room temperature with 300 nm excitation wavelength are
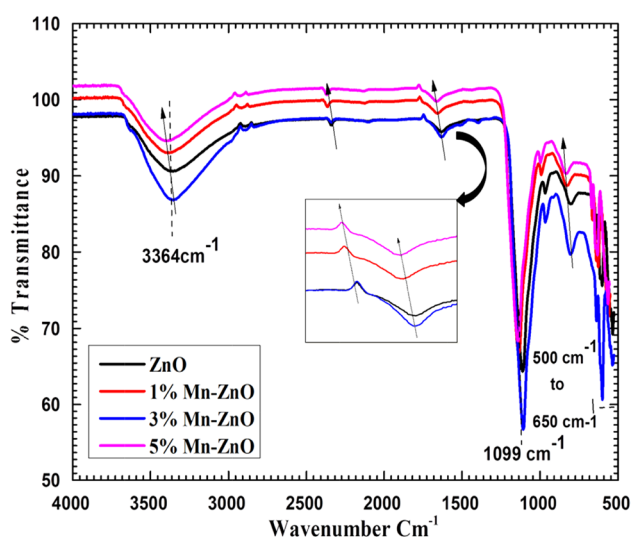
presented in Fig. 8. The PL spectra are divided into two bands, first band edge emission (NBE) rises due to recombination of electron–hole pair (free excitons) due to by exciton–exciton collision process. Second band of defect-level emission (DLE) in the visible region seems to recombination of electron–hole associated with intrinsic defects of oxygen and zinc (V_O, V_{Zn} vacancies (Singh et al. 2014)). It displays band edge emission centered near 330 nm with minor shifting in doped samples, which is of exciton radiative recombination. Another band 600 nm for all samples depicts the peak for deep level emission (DLE) of defects. The relative peak intensities for ZnO are higher as compared to and Mn-ZnO NPs. Mn insertion in ZnO lattice at particular level is effectively worked to suppress DLE, i.e., electron–hole recombination by inserting extra energy level, which also effectively decreases the band gap. While such change is also influenced by defects present in ZnO introduced by doping (Doan et al. 2014; Panigrahy et al. 2012).

DRS UV–visible and Tauc Plots Analysis

To study the optical absorption, UV–visible diffuse reflectance spectroscopy was used. The samples are taken into a chamber by sample holder without any treatment and measurements at room temperature. It can be seen from Fig. 9a that there is strong excitonic absorption peak for all prepared samples. The absorption peaks observed at 370 nm for ZnO and 375, 377, 385 nm for 1, 3 5% Mn-ZnO, respectively, that signifies red shifting toward the visible region with additional humps were observed (Kumar et al. 2017). So, it explains incorporation of Mn ions leading to a shifting
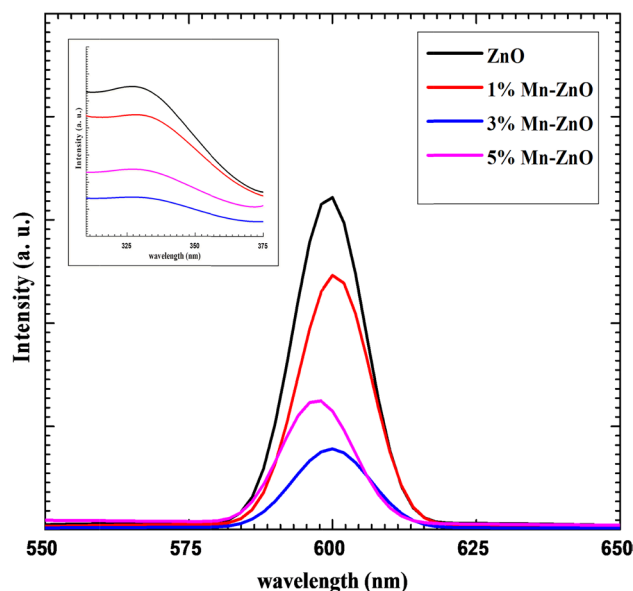

Fig. 7 ATR-FTIR spectra of ZnO and Mn-ZnO NPs with inset magnified portion

Fig. 8 Photoluminescence spectra of ZnO and Mn-ZnO NPs (excitation wavelength 300 nm)

the absorption region toward visible side that is favorable in optronic application. Such modification was further supported by measuring its energy band gap (Eg). The calculated band gaps using Tauc's formula is given in Fig. 9b. The band gap for ZnO measured to be 3.16 eV seems to lesser because of the oxygen vacancies and defects at the surface of ZnO nanocrystals. However, earlier study reveals the absorption edge is redshifted for lower Mn concentration, whereas it is blueshifted with higher Mn doping in ZnO lattice (Sharma and Jha 2017). So lower doping band gap values for 1, 3 and 5% Mn-ZnO are 2.788, 2.782 and 2.805 eV, respectively. The band gap decreases up to 3% Mn doping, while it is then slight increases for 5% Mn doping. This decrease in band gap of doped ZnO NPs is because the d-electron of Mn (t_2g levels) can easily overlap with ZnO valence band (Singh et al. 2014). The decrease in band gap also accounted theoretically and explained using the second-order perturbation theory. While 5% doping shows slight increase because of Burstein–Moss effect initiated by excess of charge carriers that pushes the Fermi level to higher energy (Abdub et al. 2012; Mondal et al. 2013; Putri et al. 2018; Viswanatha et al. 2004).

EIS Analysis

To interpret the electrical performance, the prepared film of ZnO and Mn-ZnO was employed for electrochemical impedance analysis. So for that photoanodes are immersed into tri-iodide/iodide redox couple electrolyte and performance was measured under dark. The obtained Nyquist plots are given in Fig. 10 that provides ohmic resistance (R_s) and intrinsic charge transfer resistance (R_{ct}) values found from lower and higher frequency areas. It measures the R_o values decreased from 15.98 to 15.06, 14.98, 14.6 Ω for ZnO to 1, 3, 5% Mn-doped samples. It signifies the decrease in resistance at the interface among the working electrode and electrolyte. Similarly, significant charge transfer resistance, i.e., R_{ct} value, reduced suitably to enhance the DSSCs performance. The attained values are 587.1 Ω for ZnO, while 426.3, 294.3, 327.2 Ω values imply 1, 3 and 5% values (Sharma et al. 2011; Yilmaz et al. 2019). The EIS analysis gives favorable direction for further current–voltage measurements to get better conversion efficiency results.
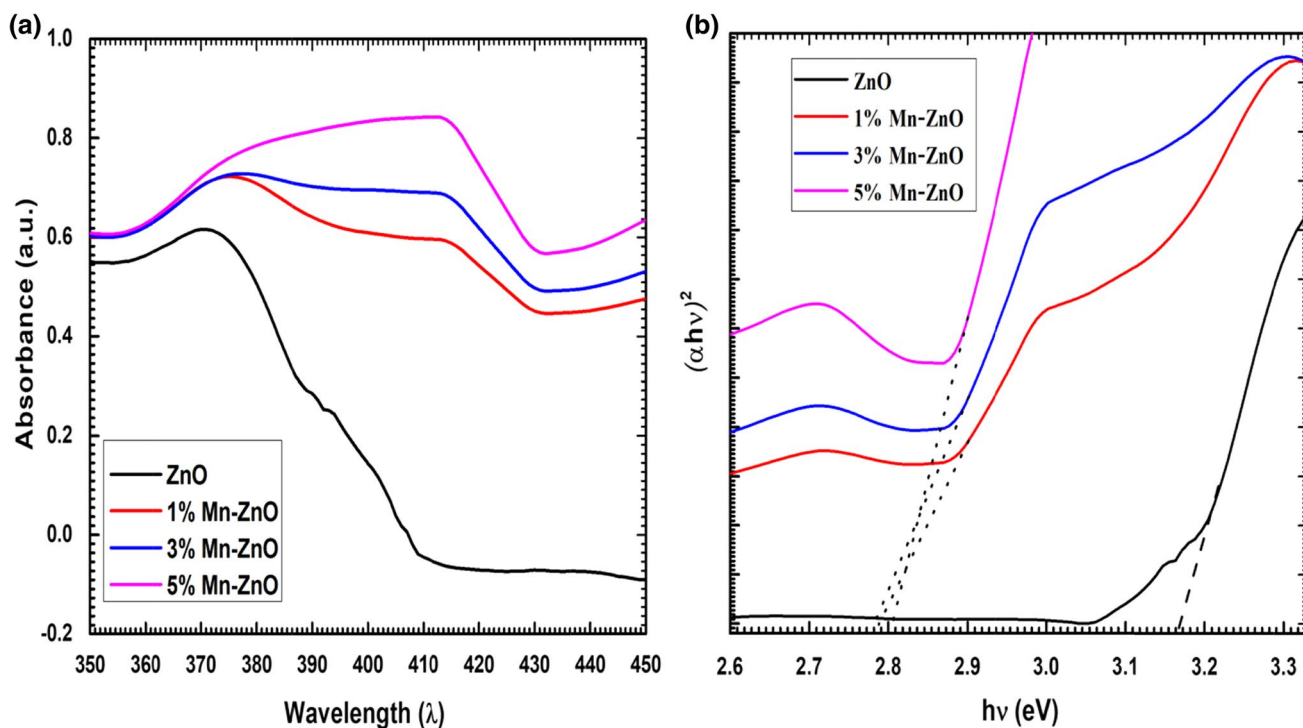

Fig. 9 (**a**) UV–visible diffuse reflectance spectra of ZnO and Mn-ZnO NPs and (**b**) Tauc plots for band gap determination
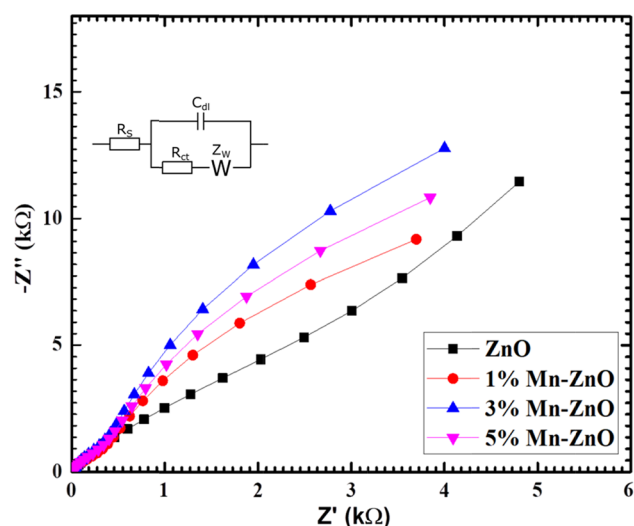
Fig. 10 Nyquist plot of the ZnO and Co-ZnO samples

Dye Preparation and its Optical Investigation

To get better output results in DSSCs, dye plays crucial role to initiate photoconversion. Usually to catch worthy results, ruthenium metal complex-based dyes, i.e., N3, N719, are used having intense absorption in UV–visible region due to metal ligand charge transfer and conjugation. For TiO$_2$-based semiconducting material, these dyes give the highest performance, while with ZnO it also provides worthy outputs but affected by stability problem. Such dyes have never been used widely due to have poisonous nature and high cost. Especially with ZnO, it forms Zn^{2+}/dye complex in acid solution that also eliminates Zn^{2+} in the lattice site. So, metal-free and highly conjugated organic dyes attracted lot of attentions of researchers. These dyes are also advantageous due to having less toxicity, abundant, low cost, higher molar excitation coefficient, tuneable optoelectronic properties (Karki et al. 2013; Vittal and Ho 2017). From variety of organic dyes, xanthene dyes appear to be beneficial because of less acidic nature, economic and greater quantum efficiencies. Xanthene dyes have xanthylium chromophoric group with amino, hydroxyl and carboxylate groups responsible for light absorption. Its molecular structure contains an highly conjugated aromatic cyclic ether with an oxygen between the two aromatic rings with intense absorption ability due to π-π* transitions. Eosin Y and Rose Bengal dye has hydroxyl and keto groups, while Rhodamine B bears keto and amino groups as anchoring groups as given in Fig. 11a. So it holds high extinction coefficients and adequate anchoring groups that would be synergistically worked to catch broad visible absorption. Also, its utilization with ZnO was enhanced by formation of stable complex with Zn^{2+} ions. Singular dyes distinctly absorb in the visible region at 518, 530 and 535 nm

as shown in Fig. 11b, which is prepared in acetonitrile and tert-butanol solutions in 1:1 proportions. So to overcome the limitation of selective absorption region or to acquire broad absorption area, we mixed these dyes in equivalent amount and formed new mixed dye likely done previously (Kumbhar et al. 2020). The absorption seems in broad region of 450 to 600 nm. Further optical absorption of films in dye was verified by immersing it into 0.3 mM dye solution for 12 h. Excess dye was removed by alcohol and studied UV−visible absorption. It reveals the better absorption after dye sensitization as given in Fig. 11c. These optimistic results are also due to better anchoring of dye on photoanode surface. The carboxylate anchoring groups mostly work well for these anchoring (Lee et al. 2018; Zhang et al. 2010). It also illustrates that Zn^{2+} is reduced by xanthene dyes, and it forms stable complex with it. So, overall ZnO and xanthene dye work co-ordinately with stability, which is impossible with ruthenium metal-based dyes (Zhang et al. 2010) (see Fig. 12).

Dye Adsorption–Desorption Study

The anchoring capacity of dye molecules on the surface of film is investigated by desorbing 1cm^2 area of dye-loaded films. Here, desorption was carried out by 5 mL aqueous solution 1 mM KOH solution. UV–Vis absorption spectra given in Fig. 3 reveal that there were different discrete absorption maxima when films were loaded with individual dye for Eosine Y, Rose Bengal and Rhodamine B dye in between 500 to 600 nm. In a similar way, the mixed 1:1:1 dye shows broad absorption range with higher absorbance. The desorption quantity from film surface is further calculated in mol/cm^2 (Delekar et al. 2018). The Eosine Y, Rose Bengal, Rhodamine B give desorbed dye amount of 2.56, 2.48 and 2.52 X 10^{-6} in mol/cm^2. However, for mixed 1:1:1 dye the amount was observed to be 3.47 × 10^{-6}, i.e., somewhat higher than individual dyes. So, the obtained results indicate that mixed dye anchors very well as compared to individual dye as mixed dye work with full of various carboxylate, hydroxyl and amine groups. So it is beneficial to use mixed dye bearing good anchoring capability to get better photoconversion results.

Construction and *I–V* Measurements of Cell

To investigate DSSCs performance of prepared photoanodes, the photoelectrochemical cell of two electrode system was constructed as given in Fig. 13, schematic diagram of DSSCs. In this system, prepared photoanodes having area of 1.0 cm^2 have used as working electrode with identical area of Pt-deposited FTO plate acting as counter electrode. While constructing, DSSCs loading of mixed dye was done by placing photoanodes in 0.3 mM dye solution for 12 h.

(a)

(b)

(c)
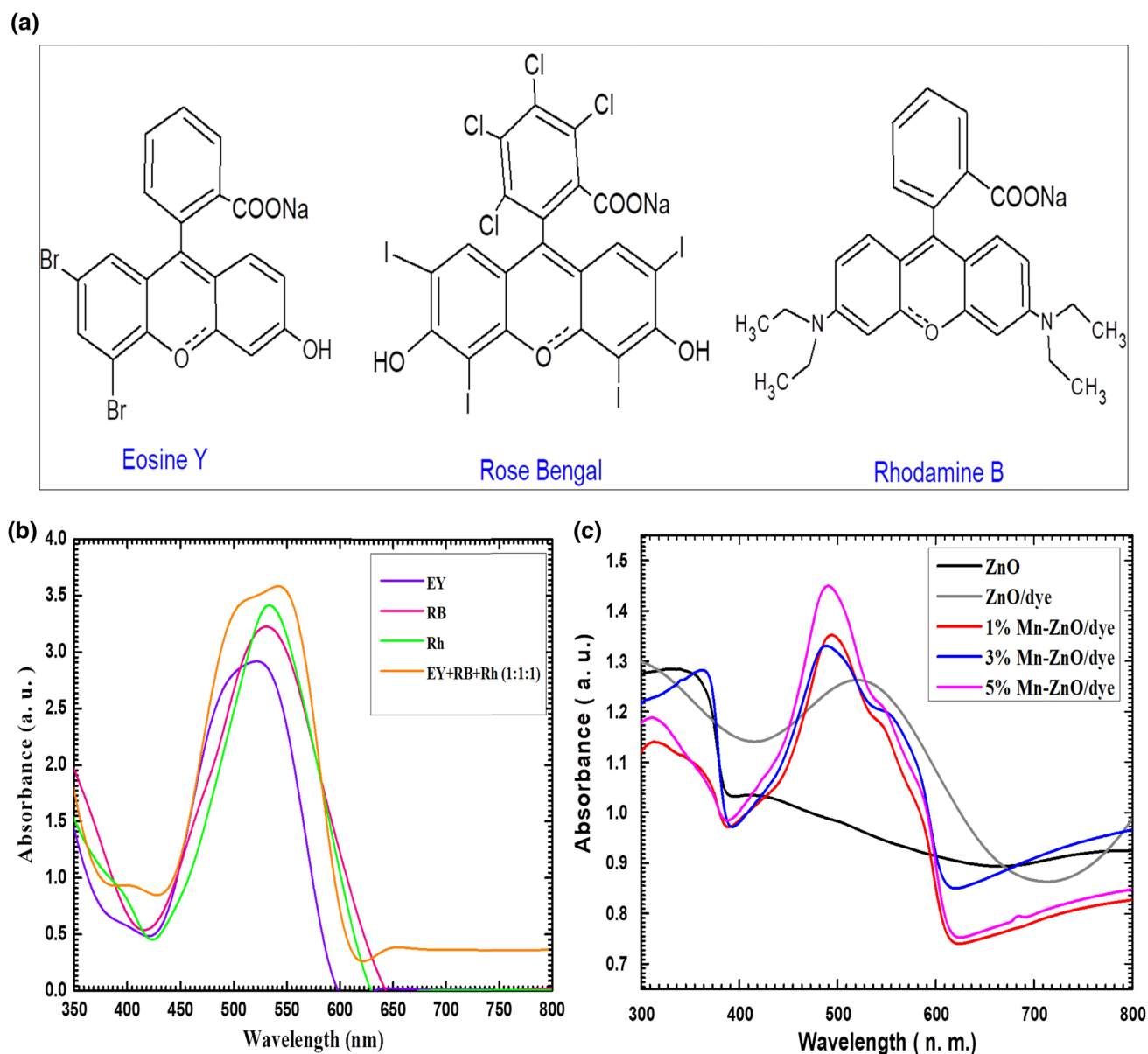
Fig. 11 (**a**) Molecular structure of xanthene dyes, (**b**) optical absorption spectra of EosineY, Rose Bengal, Rhodamine B and mixed dye in tert-butyl alcohol/acetonitrile, (**c**) UV−visible absorption spectra of Mn-ZnO photoanodes sensitized with mixed dye

The excess of sensitized dye was then removed by alcohol. For measurement, photoanode and Pt electrode are placed in electrolyte solution prepared by 0.1 M lithium iodide and 0.05 M iodine solution in propylene carbonate. After complete setup, *I-V* measurements are taken in dark and light by solar simulator under standard AM 1.5 one sun illumination (100 mW/cm^2). Here both the measurements, i.e., with and without dye sensitization, were carried out.

Photocurrent density–voltage *(I-V)* measurements of ZnO and Mn-ZnO photoanodes are recorded in Fig. 14a–d without dye sensitization and Fig. 15a–d with dye sensitization. Different parameters, i.e., V_{oc} (open-circuit voltage), (I_{sc}) short-circuit current density, FF (fill factor) and η % (efficiency in percentage), are tabulated in Table 3. The enhancement of J_{sc}, i.e., 0.065 to 0.278 mA/cm^2, was seen after sensitization of ZnO photoanode. It gives 0.036% of increase in output efficiency (η %). The
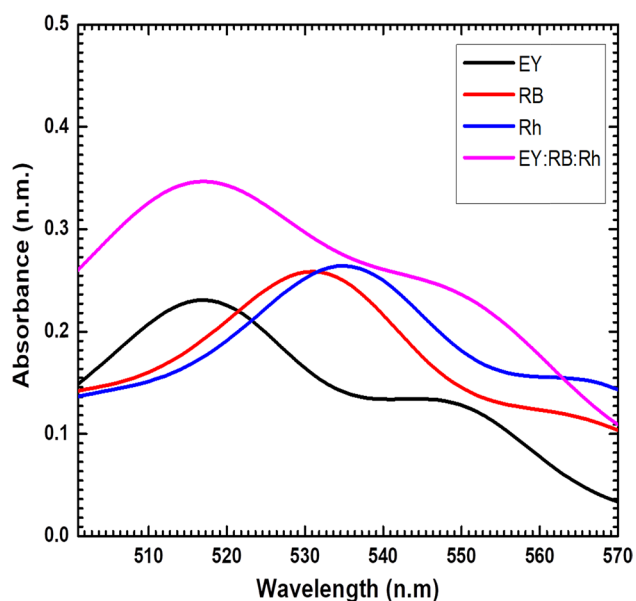
Fig. 12 UV–Vis absorption spectra of different dyes solution detached from ZnO of 1.0 cm² area

Mn-ZnO photoanodes show growth in η % till 3% (0.183 and 0.253%) doping, but it was further decreased for 5% (0.115). Such decrement attributed to higher electron–hole recombination and insignificant increment in band gap.

Conclusions

The extensive study depicts the concentration of dopant switching the entire characteristic of ZnO. The higher doping possibly shows a converse effect attributed to excessive charge carriers and electron–hole recombination. So the desirable 3% incorporation of Mn contributes to the highest output efficiency of 0.096% without dye and 0.253% with dye sensitization. The doping in ZnO varies certain structural parameters without altering its core hexagonal wurtzite structure responsible for the decrement in crystallite size defined by XRD Rietveld refinement and Raman data. The SDS surfactant well endeavored to achieve fine hexagonal particle nature was evaluated through SEM and TEM analysis. While XPS confirms the extent of Mn doping and its existence in +2 oxidation state. The mainly concerned
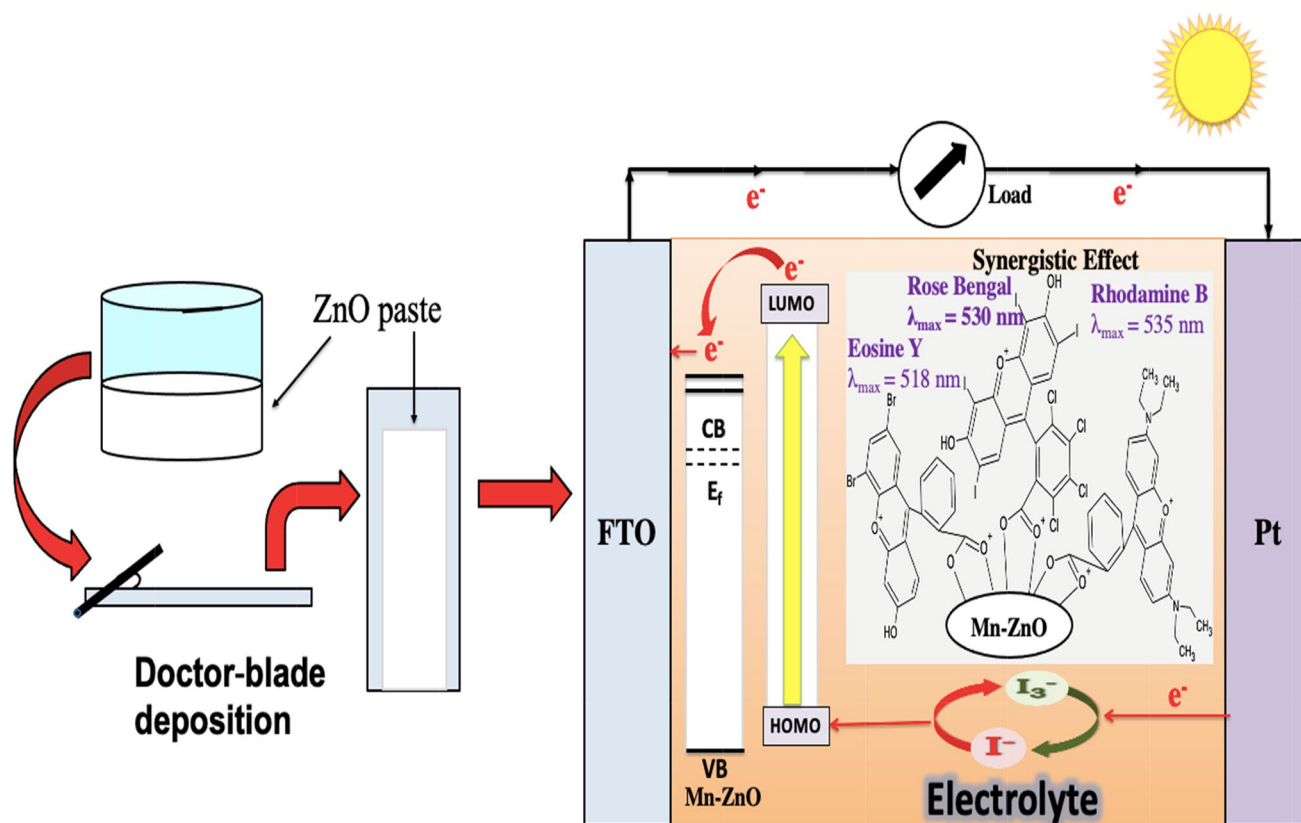

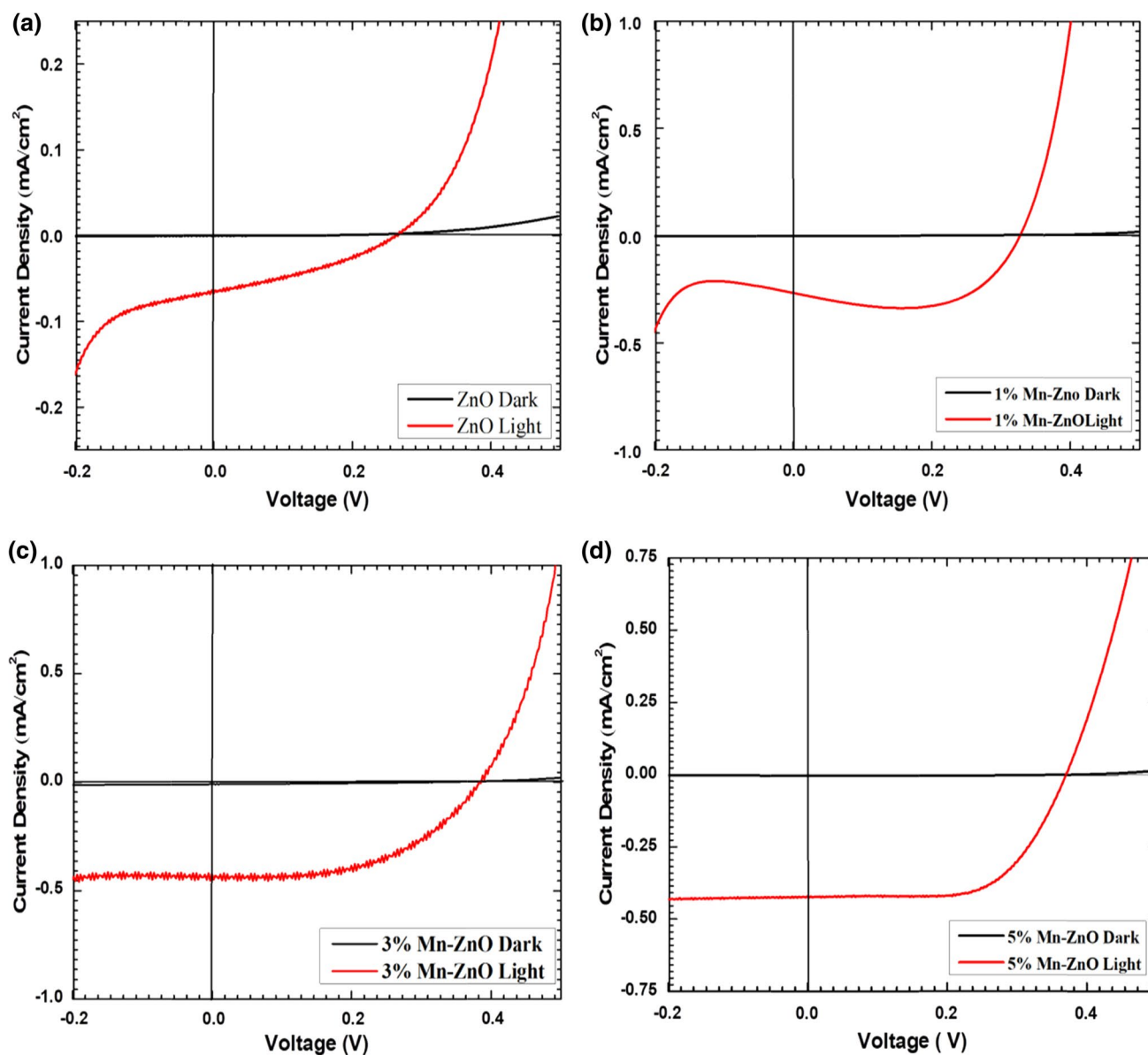**Fig. 13** Schematic diagram of DSSCs

Fig. 14 Photocurrent density–voltage (*I–V*) curves under dark and visible light for (**a**) ZnO (**b–d**) Mn-ZnO samples without dye sensitization

optical characteristic gives positive impact considerably beneficial in electrical performance. In that DRS, UV–Visible study exhibited enhanced absorption with humps that modify the band gap to lesser side calculated through Tauc plots. Finally, films prepared by doctor blade technique having hydrophilic nature promote anchoring ability of xanthene dyes analyzed in UV–Visible data. So, as far as the present scenario of DSSCs concerning ZnO is the best promising alternative to TiO_2; however, researchers are still in continuous efforts in relevant optimization of all the components to achieve the desired performance intended to commercialize in the wide market of photovoltaics. Our
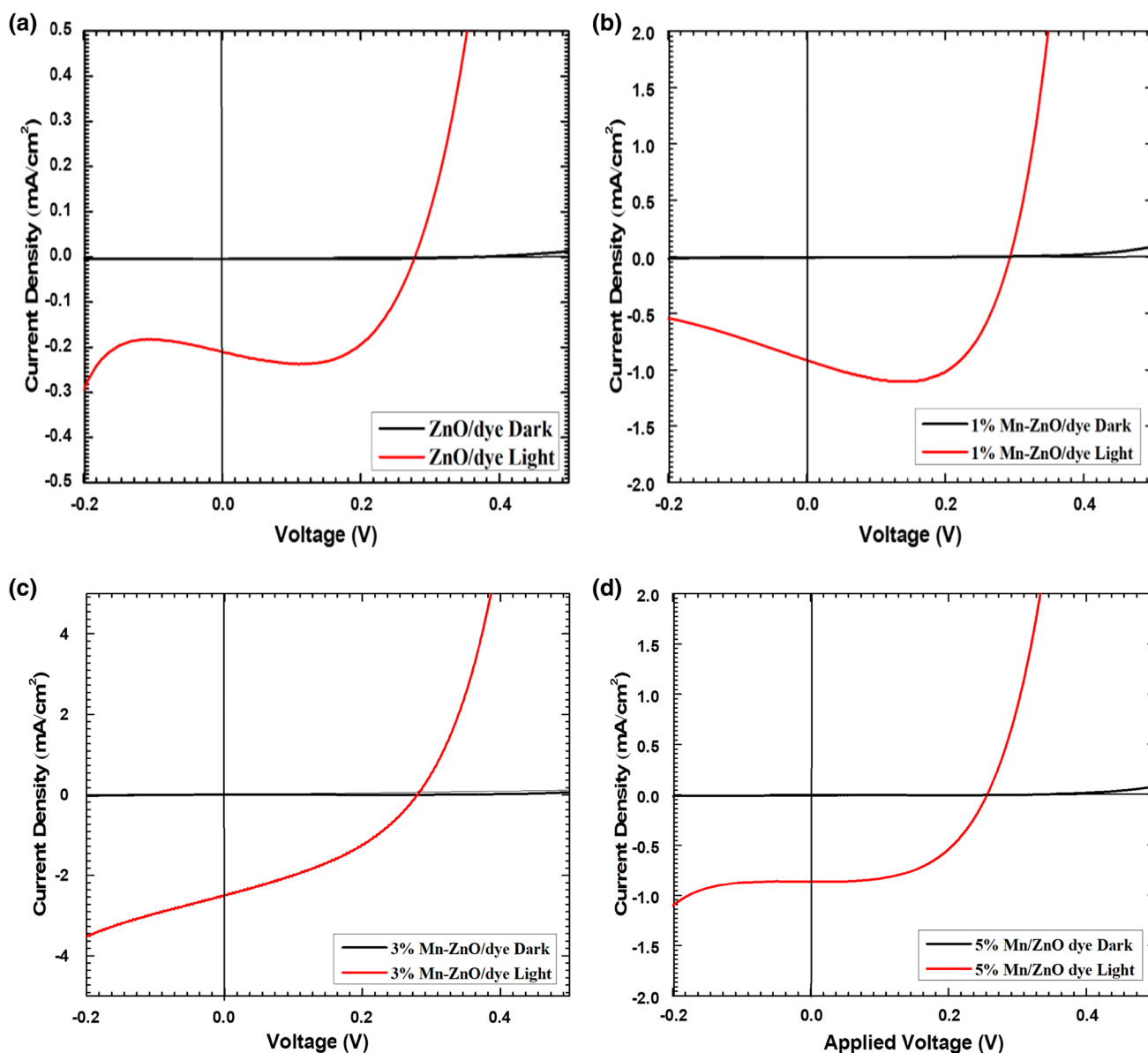
Fig. 15 Photocurrent density–voltage (*I–V*) curves under dark and visible light for (**a**) ZnO (**b–d**) Mn-ZnO samples with dye sensitization

Table 3 Photoelectrochemical parameters of the cell for ZnO and Mn-ZnO samples

Sample	Jsc (mA/cm^2) Without Dye	V_{oc} (V)	FF	η%	Jsc (mA/cm^2) With Dye	V_{oc} (V)	FF	Rs (Ω)	Rct (Ω)	η%
ZnO	0.065	0.262	0.27	0.005	0.211	0.278	0.62	16	587.1	0.036
1% Mn-ZnO	0.436	0.384	0.51	0.085	0.922	0.292	0.68	15.06	426.3	0.184
3% Mn-ZnO	0.434	0.369	0.6	0.096	2.456	0.278	0.37	14.98	294.3	0.253
5% Mn-ZnO	0.255	0.316	0.61	0.049	0.865	0.256	0.52	14.60	327.2	0.115

study highlights the use of doping and eco-friendly dye strategy unitedly to enhance the overall performance of DSSCs. Though the efficiencies are inadequate, its cost-effectiveness and environmental friendliness offer a reliable technique to grab photon flux from a wide range of solar light that converts it into electrical current.

References

Aarrestad J (1990) Simultaneous use of renewable and non-renewable natural resources. Resources and energy 12:253–262

Abdub G, Ali FBD, Hendrik C, Swart, (2012) Effect of Mn doping on the structural and optical properties of sol-gel derived ZnO nanoparticles. Cent Eur J Phys 10:478–484. https://doi.org/10.2478/s11534-011-0106-4

Aimouch D, Meskine S, Boukortt A, Zaoui A (2018) Effect of (Mn, Cr) co-doping on structural, electronic and magnetic properties of zinc oxide by first-principles studies. J Magn Magn Mater 451:70–78

Akman E (2020) Enhanced photovoltaic performance and stability of dye-sensitized solar cells by utilizing manganese-doped ZnO photoanode with europium compact layer. J Mol Liq 317:114223

Aksoy S, Polat O, Gorgun K, Caglar Y, Caglar M (2018) Li doped ZnO based DSSC: characterization and preparation of nanopowders and electrical performance of its DSSC. J Alloys Compd 739:939–94

Al-Alwani MA, Mohamad AB, Ludin NA, Kadhum AAH, Sopian K (2016) Dye-sensitised solar cells: development, structure, operation principles, electron kinetics, characterisation, synthesis materials and natural photosensitisers. Renew Sust Energ Rev 65:183–213

Ansari MS, Banik A, Kalita A, Iyer PK, Qureshi M (2018) Multifunctional hierarchical 3-D ZnO superstructures directly grown over FTO glass substrate: enhanced photovoltaic and selective sensing applications. J Mater Chem A 1:1–23

Badawy WA (2015) A review on solar cells from Si-single crystals to porous materials and quantum dots. J Adv Res 6:123–132

Bhakat C, Singh PP (2012) Zinc oxide nanorods: synthesis and its applications in solar cell International. J Mod Eng Res 2:2452–2454

Bhardwaj R, Bharti A, Singh JP, Chae KH, Goyal N, Gautam S (2018) Structural and electronic investigation of ZnO nanostructures synthesized under different environments. Heliyon 4:594

Bonifácio MAR, Lira H, d L, Neiva LS, Kiminami R H, Gama L, (2017) Nanoparticles of ZnO Doped With Mn: structural and morphological characteristics. J Mater Res 20:1044–1049

Deepak K, Sarita K, Sagar D, Rekha N, Avinash N (2019) Photoelectrochemical cell performance Cu doped ZnO photoanode sensitized by xanthene dyes. Nanosyst Phys Chem Math 10:466–474

Delekar SD, Dhodamani AG, More KV, Dongale TD, Kamat RK, Acquah SF, Dalal NS, Panda DK (2018) Structural and optical properties of nanocrystalline TiO₂ with multiwalled carbon nanotubes and its photovoltaic studies using Ru (Ii) sensitizers. ACS Omega 3:2743–2756

Doan MT, Ho XV, Nguyen T, Nguyen VN (2014) Influence of doping Co to characterization of ZnO nanostructures. Adv Nat Sci Nano Nanotech 5:025011

Fabbiyola S, Kennedy LJ (2019) Bandgap engineering in Doped ZnO nanostructures for dye sensitized solar cell applications. J Nanosci Nanotech 19:2963–2970

Fakharuddin A, Jose R, Thomas M, Brown T, Fabregat-Santiagoc F, Bisquert J (2014) A perspective on the production of dye-sensitized solar modules. Energy Environ Sci 7:3952–3981

Felipe A, Fonseca VD, Siqueira RL, Landers R, Ferrari JL, Marana NL, Sambrano JR, La Porta FA, Schiavon MA (2018) A theoretical and experimental investigation of Eu-doped ZnO nanorods and its application on dye sensitized solar cells. J Alloys Compd 739:939–947

Ganesh RS et al (2017) Low temperature ammonia gas sensor based on Mn-doped ZnO nanoparticle decorated microspheres. J Alloys Compd 721:182–190

Grandell L, Lehtilä A, Kivinen M, Koljonen T, Kihlman S, Lauri LS (2016) Role of critical metals in the future markets of clean energy technologies. Renew Energy 95:53–62

Green MA (2002) Third generation photovoltaics: solar cells for 2020 and beyond. Physica E Low Dimens Syst Nanostruct 14:65–70

Guillén E, Peter LM, Anta J (2011) Electron transport and recombination in ZnO-based dye-sensitized solar cells. J Phys Chem C 115:22622–22632

Hao Y-M, Lou S-Y, Zhou S-M, Yuan R-J, Zhu G-Y, Li N (2012) Structural, optical, and magnetic studies of manganese-doped zinc oxide hierarchical microspheres by self-assembly of nanoparticles. Nanoscale Res Lett 7:100

Jayachandraiah C, Krishnaiah G (2017) Influence of cerium dopant on magnetic and dielectric properties of ZnO nanoparticles. J Mater Sci 52:7058–7066

Jayakumar O, Salunke H, Kadam R, Mohapatra M, Yaswant G, Kulshreshtha S (2006) Magnetism in Mn-doped ZnO nanoparticles prepared by a co-precipitation method. Nanotechnology 17:1278

Jayanthi K, Chawla S (2010) Synthesis of Mn doped ZnO nanoparticles with biocompatible capping. Appl Surf Sci 256:2630–2635

Karki I, Nakarmi J, Mandal P, Chatterjee S (2013) Effect of organic dyes on the performance of ZnO based dye-sensitized solar cells. Appl Sol Energy 49:40–45

Khan M, Al-Mamun M, Halder P, Aziz M (2017) Performance improvement of modified dye-sensitized solar cells. Renew Sust Energ Rev 71:602–617

Kim J-W, Lee SJ, Biswas P, Lee TI, Myoung J-M (2017) Solution-processed n-ZnO nanorod/p-Co3O4 nanoplate heterojunction light-emitting diode. Appl Surf Sci 406:192–198

Kim J-H, Lee K-J, Roh J-H, Song S-W, Park J-H, Yer I-H, Moon B-M (2012) Ga-doped ZnO transparent electrodes with TiO₂ blocking layer/nanoparticles for dye-sensitized solar cells. Nanoscale Res Lett 7:11

Kumar KA, Amanchi SR, Sreedhar B, Ghosal P, Subrahmanyam C (2017) Phenol and Cr (VI) degradation with Mn ion doped ZnO under visible light photocatalysis. RSC Adv 7:43030–43039

Kumar V, Singh N, Kumar V, Purohit LP, Kapoor A, Ntwaeaborwa OM, Swart HC (2013) Doped zinc oxide window layers for dye sensitized solar cells. J Appl Phys 114:134506–134516

Kumbhar D, Kumbhar S, Dhodamani A, Delekar S, Harale N, Nalawade R, Nalawade A (2020) Enhanced photoelectrochemical cell performance of Co doped ZnO nanoparticles sensitized by affordable mixed dyes as sensitizer. Inorg Nano-Met Chem 1–14. https://doi.org/10.1080/24701556.2020.1835963

Lanjewar M, Gohel JV (2017) Enhanced performance of Ag-doped ZnO and pure ZnO thin films DSSCs prepared by sol-gel spin coating. Inorg Nano-Met Chem 47:1090–1096

Lee H, Kim J, Kim DY, Seo Y (2018) Co-sensitization of metal free organic dyes in flexible dye sensitized solar cells. Org Electron 52:103–109

Li G et al (2009) Synergistic effect between anatase and rutile TiO₂ nanoparticles in dye-sensitized solar cells. Dalton Trans 7:10078–10085

Liu Q et al (2014) Direct conversion of two-dimensional ZIF-L film to porous ZnO nano-sheet film and its performance as photoanode in dye-sensitized solar cell. Micropor Mesopor Mat 194:1–7

Liu W, Tang X, Tang Z (2013) Effect of oxygen defects on ferromagnetism of Mn doped ZnO. J Appl Phys 114:123911

López R et al (2017) Low-temperature oxidation effects on the morphological and structural properties of hexagonal Zn nanodisks. Rev Mex de Fis 63:308–313

Mahmood K, Jin Sung H (2014) A dye-sensitized solar cell based on a boron-doped ZnO (BZO) film with double light-scattering-layers tructured photoanode. J Mater Chem A 2:5408–5417

Mahroug A, Amari R, Boukhari A, Deghfel B, Guerbous L, Selmi N (2018) Synthesis, structural, morphological, electronic, optical and luminescence properties of pure and manganese-doped zinc oxide nanostructured thin films: effect of doping. J Nanoelectron Optoelectron 13:732–742

Mao Y et al (2014) Effect of Mn doping on the microstructures and sensing properties of ZnO nanofibers. Appl Surf Sci 298:109–115

Mittal M, Sharma M, Pandey O (2016) Fast and quick degradation properties of doped and capped ZnO nanoparticles under UV–Visible light radiations. Sol Energy 125:51–64

Mondal S, Bhattacharyya S, Mitra P (2013) Preparation of manganese-doped ZnO thin films and their characterization. Bull Mater Sci 36:223–229

Nithya R, Kannan A, Manjulavalli (2015) Investigation of pure and transition metal doped ZnO nanoparticles for photovoltaic applications. Int J Chem Tech Res 7:1178–1184

O'Regan B, Grätzel M (1991) A low-cost, high-efficiency solar cell based on dye-sensitized colloidal TiO_2 films. Nature 353:737–740

Panigrahy B, Aslam M, Bahadur D (2012) Effect of Fe doping concentration on optical and magnetic properties of ZnO nanorods. Nanotechnology 23:115601

Parthibavarman M, Jayashree M, Sharmila V (2016) Tunable of optical and electrical properties for pure and Mn doped ZnO nanoparticles. Int J Multidisciplinary Res Rev 1:231–235

Paul R, Gayen R, Biswas S, Bhat SV, Bhunia R (2016) Enhanced UV detection by transparent graphene oxide/ZnO composite thin films. RSC Adv 6:61661–61672

Ponnusamy R, Selvaraj SC, Ramachandran M, Murugan P, Nambissan PMG, Sivasubramanian D (2016) Diverse spectroscopic studies and first-principles investigations of the zinc vacancy mediated ferromagnetism in Mn-doped ZnO nanoparticles. Cryst Growth Des 16:3656–3668

Putri NA, Fauzia V, Iwan S, Roza L, Umar AA, Budi S (2018) Mn-doping-induced photocatalytic activity enhancement of ZnO nanorods prepared on glass substrates. Appl Surf Sci 439:285–297

Raj CJ, Prabakar K, Karthick S, Hemalatha K, Son M-K, Kim H-J (2013) Banyan root structured Mg-doped ZnO photoanode dye-sensitized solar cells. J Phys Chem C 117:2600–2607

Rekha K, Nirmala M, Nair MG, Anukaliani A (2010) Structural, optical, photocatalytic and antibacterial activity of zinc oxide and manganese doped zinc oxide nanoparticles. Physica B Condens Matter 405:3180–3185

Sabri NS, Yahya AK, Talari MK (2012) Emission properties of Mn doped ZnO nanoparticles prepared by mechanochemical processing. J Lumin 132:1735–1739

Sengupta D, Das P, Mondal B, Mukherjee K (2016) Effects of doping, morphology and film-thickness of photo-anode materials for dye sensitized solar cell application - A review. Renew Sust Energ Rev 60:356–376

Shatnawi M, Alsmadi AM, Bsoul I, Salameh B, Mathai M, Alnawashi G, Gassem M, Alzoubi M, Al-Dweri F, Bawa'aneh MS (2016) Influence of Mn doping on the magnetic and optical properties of ZnO nanocrystalline particles. Results Phys 6:1064–1071

Sharma D, Jha R (2017) Transition metal (Co, Mn) Co-Doped Zno nanoparticles: effect on structural and optical properties. J Alloys Compd 698:532–538

Sharma S, Siwach B, Ghoshal S, Mohan D (2017) Dye sensitized solar cells: from genesis to recent drifts. Renew Sust Energ Rev 70:529–537

Sharma M, Gayen R, Pal A, Kanjilal D, Chatterjee R (2011) Complex impedance spectroscopy of Mn-doped zinc oxide nanorod films. Solid State Commun 151:1182–1187

Sharma R, Patel S, Pargaien K (2012) Synthesis, characterization and properties of Mn-doped ZnO nanocrystals. Adv Nat Sci Nanosci Nanotechnol 3:035005

Shohany BG, Motevalizadeh L, Abrishami ME (2018) Investigation of Zno thin-film sensing properties for CO_2 Detection: effect of Mn doping. J Theor Appl Phys 12:219–225

Shrama SK, Saurakhiya N, Barthwal S, Kumar R, Sharma A (2014) Tuning of structural, optical, and magnetic properties of ultrathin and thin ZnO nanowire arrays for nano device applications. Nanoscale Res Lett 9:122

Singh AK, Thool GS, Bangal PR, Madhavendra SS, Singh SP (2014) Low temperature Mn doped ZnO nanorod array: synthesis and its photoluminescence behavior. Ind Eng Chem Res 53:9383–9390

Singh B, Shrivastava S, Ganesan V (2017) Effects of Mn doping on Zinc Oxide films prepared by spray pyrolysis technique. Int J Nanosci 16:1650024

Shah SM, Naz H, Ali RN, Alam F, Ali A, Farooq M, Shaha A, Badshah A, Siddiq M, Waseem A (2017) Optical and morphological studies of transition metal doped ZnO nanorods and their applications in hybrid bulk heterojunction solar cells. Arab J Chem 10:1118–1124

Shusma C, Girish Kumar S (2017) Advancements in the zinc oxide nanomaterials for efficient photocatalysis. Chem Pap 71:2023–2042

Son YJ, Kang JS, Yoon J, Kim J, Jeong J, Kang J, Lee MJ, Park HS, Sung Y-E (2018) Influence of TiO2 particle size on dye-sensitized solar cells employing an organic sensitizer and a cobalt (III/II) redox electrolyte. J Phys Chem C 122:7051–7060

Tao R, Tomita T, Wong RA, Waki K (2012) Electrochemical and structural analysis of Al-doped ZnO nanorod arrays in dye-sensitized solar cells. J Power Sources 214:159–165

Ton-That C, Foley M, Phillips MR, Tsuzuki T, Smith Z (2012) Correlation between the structural and optical properties of Mn-doped ZnO nanoparticles. J Alloys Compd 522:114–117

Tuyen NV, Long NN, Quyhn Hoa TT, Nghia NX, Chi DH, Higashimine K, Mitani T, Cahn TD (2009) Indium-doped zinc oxide nanometre thick disks synthesised by a vapour-phase transport process. J Exp Nanosci 4:243–252

Undre PG, Birajdar SD, Kathare R, Jadhav K (2018) Enhancement of Electrical Resistivity in Nickel Doped ZnO Nanoparticles. Procedia Manuf 20:477–480

Van Zalk J, Behrens P (2018) The spatial extent of renewable and non-renewable power generation: A review and meta-analysis of power densities and their application in the US. Ener policy 123:83–91

Vittal R, Ho K-C (2017) Zinc oxide based dye-sensitized solar cells: A review. Renew Sust Energ Rev 70:920–935. https://doi.org/10.1016/j.rser.2016.11.273

Viswanatha R, Sapra S, Sen Gupta S, Satpati B, Satyam P, Dev B, Sarma D (2004) Synthesis and characterization of Mn-doped Zno nanocrystals. J Phys Chem B 108:6303–6310

Yang S, Zhang Y (2013) Structural, optical and magnetic properties of Mn-doped ZnO thin films prepared by sol–gel method. J Magn Magn Mater 334:52–58

Ye N, Qi J, Qi Zi, Xiaomei Z, Ya Y, Jing L, Yue Z (2010) Improvement of the performance of dye-sensitized solar cells using Sn-doped ZnO nanoparticles. J Power Sourc 195:5806–5809

Ye M, Wen X, Wang M, Iocozzia J, Zhang N, Lin C, Lin Z (2015) Recent advances in dye-sensitized solar cells: from photoanodes, sensitizers and electrolytes to counter electrodes. Mater Today 18:155–162

Yilmaz M, Çinar Demir K, Turgut G, Aydogan S (2019) Electrochemical impedance spectroscopy analysis of ZnO films: the effect of Mg doping. Philos Mag Lett 99:243–252

Zhang J, Sun L, Ichinose K, Funabiki K, Yoshida T (2010) Effect of anchoring groups on electrochemical self-assembly of ZnO/xanthene dye hybrid thin films. Phys Chem Chem Phys 12:10494–10502